Multidimensional Systems and Signal Processing, 14, 49–82, 2003

Detection and Analysis of Anisotropic Scattering in SAR Data☆

ANDREW J. KIM ajkim@alum.mit.edu
Stochastic Systems Group, Massachusetts Institute of Technology, Cambridge, MA 02139

JOHN W. FISHER III
Stochastic Systems Group, Massachusetts Institute of Technology, Cambridge, MA 02139

ALAN S. WILLSKY[1]
Stochastic Systems Group, Massachusetts Institute of Technology, Cambridge, MA 02139

Received December 1, 2000; Revised September 9, 2001; Accepted September 26, 2001

Abstract. Scattering from man-made objects in SAR imagery exhibits aspect and frequency dependencies which are not well modeled by standard SAR imaging techniques. If ignored, these deviations will reduce recognition performance due to the model mismatch, but when appropriately accounted for, these deviations from the ideal point scattering model can be exploited as attributes to better distinguish scatterers and their respective targets. With this premise in mind, we have developed an efficient modeling framework that incorporates scatterer anisotropy. One of the products of our analysis is the assignment of an anisotropy label to each scatterer conveying the degree of anisotropy. Anisotropic behavior is commonly predicted for geometric scatterers (scatterers with a simple geometric structure), but it may also arise from volumetric scatterers (random arrangements of interfering point scatterers). Analysis of anisotropy arising from these two modalities shows a clear source-dependent relationship between the anisotropy classification and parameters of the scatterer. In particular, the degree of anisotropy is closely related to the size of the scatterer, and increasing the aperture size reduces the incidence of volumetric anisotropy but preserves the detection rate for geometric anisotropy. This result helps to address the question in the SAR community regarding the utility of wide-aperture SAR data for ATR since wide-aperture data reveals geometric anisotropy while resolving volumetric anisotropy into individual isotropic scatterers.

Key Words: SAR, anisotropy, wide-aperture, multi-resolution, canonical scattering, volumetric scattering, ATR

1. Introduction

Scatterers composing a target in synthetic aperture radar (SAR) imagery often exhibit nonideal scattering behavior in the form of aspect and frequency dependence, particularly in wide-aperture or wide-band data. Standard SAR image formation ignores this model deviation resulting in suboptimal use of the data. The modeling error may furthermore

☆ This work is sponsored by Air Force Office of Scientific Research grant F49620-96-1-0028 (subcontract BU GC123919NGD), Office of Naval Research grant N00014-00-1-0089, and DARPA under Wright Patterson grant F33615-97-1014.

introduce artifacts, such as peak scatterer instability, which unnecessarily complicate the recognition problem. These deviations from the ideal point scattering model should not be viewed as a nuisance and approximated away, but they should instead be seen as a useful attribute which can be used to distinguish scatterers and thus their respective targets. In this paper, we present a multi-scale analysis for detecting and classifying scatterer anisotropy in SAR data. This analysis is used for (i) studying the dependence of the proposed anisotropy attribution on scatterer phenomenology and (ii) assessing the utility of wide-aperture data in the attribution process and hence for automatic target recognition (ATR).

There are numerous benefits to knowing the anisotropy of a scatterer which the standard image formation process ignores. From an imaging standpoint, a better scattering model allows for more accurate reflectivity estimates since the weighting in the coherent averaging can be adjusted according to the azimuthal scattering pattern (e.g. with a matched filter) such as in the work done by Allen et al. [1] and by Chaney et al. [2]. Knowledge of anisotropy may also be used to better suppress interfering scatterers in a super-resolution image formation algorithm such as Capon's method [3] or the high definition imaging proposed by Benitz et al. [4], [5]. In addition to improving reflectivity estimation, knowledge of a scatterer's anisotropy is useful as a feature in and of itself. For a canonical scatterer, one can infer properties about its geometric shape and size from the observed anisotropy. For instance, a flat plate produces a strong specular response where the degree of specularity is directly related to the size of the plate in cross-range. A sphere however produces an isotropic response regardless of the size of the sphere. Knowledge of the geometry of the individual scatterers on an object may then be considered as a group to aid the classification of the target under investigation as described in [9], [10], [11]. Anisotropy information may also be of use in characterizing the stability of a scatterer. In particular, one would expect the specular response from an anisotropic canonical scatterer to appear only over a small range in azimuth leading to an observability that is highly sensitive to azimuthal orientation. Knowledge of the anisotropy however allows such sensitivity to be incorporated into algorithms, such as peak matching, which would improve ATR performance.

The focus of this paper is to present a method for classifying anisotropy and to study behavior of the attribution under different conditions. The analysis presented here is based on a general characterization of azimuthal anisotropy which is not tuned to a particular canonical scatterer. The basis of our analysis is the sub-aperture pyramid which is a set of sub-apertures arranged in a pyramidal fashion. The collection of sub-apertures provides a multi-resolution representation of SAR data. These multiple apertures allow for the observation of varying degrees of azimuthal anisotropy which are unobservable under standard SAR image formation. With this pyramidal representation of the data, we propose a hypothesis test for anisotropy which measures the concentration of scattering energy across the aperture.

Analysis of this characterization reveals aspects of the phenomenology associated with anisotropy and how the attribution can be utilized in ATR. In studying the behavior of our anisotropy characterization, we consider two well known sources of anisotropy: geometric and volumetric scatterers. Scattering models such as physical

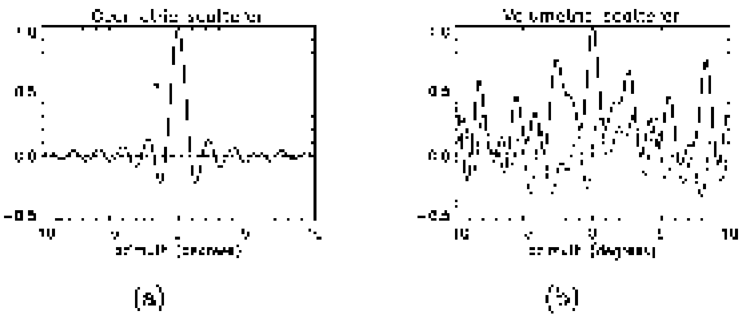

Figure 1. Instances of azimuthal scattering by a (a) geometric scatterer and (b) volumetric scatterer with the real and imaginary components of the response shown in the solid and dashed lines respectively.

optics and the Geometric Theory of Diffraction (GTD) give functional forms for radar scattering from canonical scatterers which clearly convey an azimuthal dependence on the shape, size, and orientation of a scatterer. These models are based on very specific assumptions about the configuration of scatterer, such as equal-sized plates in a dihedral or pairwise orthogonality of plates in a trihedral. As our analysis is concerned with producing a general characterization of anisotropy, we will not entangle ourselves with such fine structural details. This approach allows us to consider the broader class of what we call *geometric scatterers* which include not only canonical scatterers but also scatterers that deviate from canonicity. Besides geometric scatterers, anisotropy may also arise from a *volumetric scatterer* which is a collection of closely located point scatterers that interfere with each other. The anisotropy exhibited by volumetric scatterers, however, is not as stable as the anisotropy produced by geometric scatterers. As an example, Figure 1 shows the azimuthal response from a canonical flat plate measuring 1m in cross-range and a volumetric scatterer composed of 10 randomly located point scatterers distributed over 1m in cross-range. The flat plate response is clearly anisotropic. The volumetric scatterer is also anisotropic, but to a lesser degree as the scatterer's energy is more distributed across the aperture. As hinted to in Figure 1, the behavior between geometric and volumetric anisotropy[2] is different and ultimately leads to an ability to distinguish between the two sources of anisotropy to a degree. This distinction is highly desirable since it will then allow for tailored use of the anisotropy information based on the source. In particular, for geometric scatterers, we can infer physical properties of the scatterer and a high degree of stability, while for volumetric scatterers, we can infer the spatial support of the collection of scatterers and a low degree of stability.

The remainder of this paper elaborates on the ideas presented above. Section 2 presents the multi-resolution sub-aperture pyramid used to represent the SAR data. Section 3 then describes the set of hypotheses that we consider and develops the hypothesis tests on the sub-aperture pyramid. Section 4 presents experimental analysis demonstrating the utility of the anisotropy attribution and in particular the attribution's

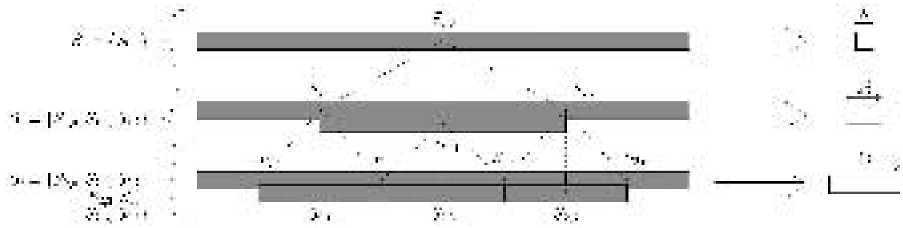

Figure 2. Illustration of the three level, half-overlapping, half-aperture pyramid. Left: Sub-apertures composing the pyramid. Right: Resolution cell size associated with reflectivity estimates formed from sub-apertures at the

relation to the scatterer phenomenology. The paper concludes with a summary and discussion in Section 5.

2. Sub-Aperture Analysis

The foundation of our analysis is the sub-aperture pyramid which we present in this section. This structure is motivated by the scattering physics involved in SAR and presents the data in a way that allows for simple and intuitively reasonable hypothesis tests. Because of the linear structure of the aperture, we associate it with an interval of the real line throughout this paper. In particular, the full-aperture is denoted by the interval $[0, 1) = \{t|0 \leq t < 1\}$.

2.1. Definition

The intuitive idea of the sub-aperture pyramid is to generate an over-complete covering of the full-aperture with sub-apertures that can be arranged in a pyramidal structure. These sub-apertures will be used both to form our reflectivity estimates and to represent our set of candidate anisotropy hypotheses. The prototypical sub-aperture covering that we use throughout this paper is the half-overlapping, half-aperture pyramid shown in Figure 2.

Formally, we take a sub-aperture pyramid to be a set S of sub-apertures with the following structure. The set S is partitioned into smaller sets S_m all the elements of which have a particular sub-aperture length as illustrated in Figure 2. S_0 refers to the set consisting of the largest sub-apertures, and S_M refers to the set of the smallest sub-apertures. A second subscript on S denotes a specific sub-aperture at the given scale. Note that any sub-aperture can be used to form a SAR image. The images formed with a smaller value of m, i.e. with a larger aperture, have a finer cross-range imaging resolution because of the inverse relationship between resolution cell size and aperture length. This point is illustrated in Figure 2 where if the full-aperture produces a resolution cell of size δ, then the half and quarter-apertures produce resolution cells of sizes 2δ and 4δ, respectively. Note that this inverse relationship between sub-aperture size and resolution cell size may lead to ambiguity when terms such as "coarse" and "fine" are used. For instance, a "coarser" (i.e. larger) sub-aperture produces a "finer" resolution cell. To avoid any ambiguity, we will explicitly use the terms "smaller" and "larger" when referring to sub-aperture sizes and the terms "finer" and "coarser" when referring to resolution cell sizes.

The idea of the sub-aperture pyramid is to present SAR data in an over-complete representation at a variety of cross-range resolution versus azimuthal[3] resolution trade-offs. Recall that cross-range resolution is inversely proportional to aperture length. Thus, at lower levels of the sub-aperture pyramid, spatial resolution has been exchanged for azimuthal resolution, i.e. the ability to better observe anisotropic phenomena. This is the classic time–frequency resolution tradeoff in Fourier analysis, and each level of the pyramid represents the data under a particular cross-range–azimuth resolution. The presence of multiple resolutions is attractive because we expect the best representation to depend on the underlying anisotropy. In particular, it is the set which has the sub-aperture which best captures the scattering energy with minimal aperture length, i.e. the closest resemblance to a matched-filter using an indicator function over a sub-aperture. Since the scatterer anisotropy (and thus best sub-aperture representation) cannot be known apriori, an over-complete basis, such as that provided by the sub-aperture pyramid, is useful in finding the best representation.

Having conveyed the intuition behind the sub-aperture pyramid, we now establish the necessary conditions on the pyramid for what follows later. In particular, the following conditions are imposed on S:

(A) $\forall S_{m,i}$, $S_{m,i} \subset [0, 1)$,
(B) $\forall S_{m,i}$, $\exists$ a partition $\mathcal{P}(m, i) \subset S_M$ of $S_{m,i}$, and
(C) $\forall S_{m,i}$ with $m \geq 1$, $\exists S_{m-1,j}$ such that $S_{m,i} \subset S_{m-1,j}$.

The first condition simply restricts the sub-apertures to be a subset of the available aperture. Motivated by our search for concentrated unimodal scattering in azimuth, we only consider the special case where each sub-aperture is a connected interval. Moreover, we also assume that $S_{0,0}$ is the full-aperture to allow for consideration of the minimal degree of anisotropy and allow for the finest imaging resolution permissible. The second condition insures that each sub-aperture can be represented by a partition of smallest-sized sub-apertures. This condition will allow for the set of measurements obtained from S_M to form a sufficient statistic for all the measurements in S. Thus, although other sub-aperture measurements will be referred to in this paper for intuition and interpretation, all computation can be done using only measurements from the smallest sub-apertures. The third condition asserts that each sub-aperture, except those in S_0, has a parent sub-aperture which contains it. This last condition is not a fundamentally necessity for our anisotropy analysis, however, we use this condition because it permits us to construct an intuitive telescopic hypothesis test on a tree which will not only afford computational efficiency but also robustness. Herein, the term *sub-aperture pyramid* refers to one satisfying conditions (A)–(C).

Now, focusing our attention on a particular location in the scene, each sub-aperture $S_{m,i}$ can be used to generate an associated reflectivity measurement $q_{m,i}$. The collection of

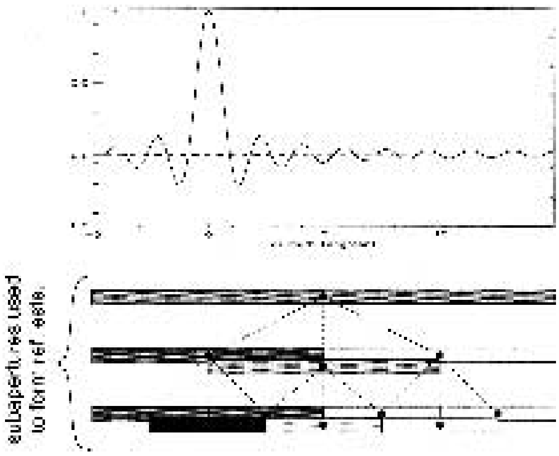

Figure 3. The response of a $1m \times 1m$ flat plate and a depiction of the reflectivity estimate for each of the sub-apertures. Darker shaded sub-apertures convey larger reflectivity estimates.

reflectivity measurements from the different offset sub-apertures in S_M are formed into a vector which is denoted by $\boldsymbol{q}_M$. The measured sub-aperture reflectivity $q_{m,i}$ is obtained in the same fashion as in standard SAR image formation, i.e.

$$q_{m,i} = \int_{S_{m,i}} a(t)dt \tag{1}$$

where $a(t)$ is the azimuthal response of the scatterer[4]. Although reflectivity measurements from smaller sub-apertures have an associated coarser resolution, they are less susceptible to azimuthal variations and provide a means for measuring scattering energy across the aperture. Note that the measured reflectivity is *not* normalized with respect to the sub-aperture length[5]. Thus, when interested in the actual reflectivity estimate, one should divide the measured sub-aperture reflectivity $q_{m,i}$ by the sub-aperture length $L_{m,i} = \lambda(S_{m,i})$, where λ denotes Lebesgue measure.

2.2. Interpretation and Motivation

Different types and sizes of geometric scatterers exhibit different aspect dependencies. The motivation for using the sub-aperture pyramid is that the pyramid is expected to reveal distinguishing aspect dependences in the scattering. For example, a metal sphere has a strong response in all directions and thus produces a strong consistent reflectivity estimate from each of the sub-apertures. However, as depicted in Figure 3, a flat plate produces a specular response which is significantly stronger when oriented broadside with respect to the radar. Thus, the reflectivity estimates vary across the sub-apertures with the largest estimate coming from the sub-aperture oriented broadside to the plate. Furthermore, because various sized sub-apertures are used, the duration of the broadside flash is also

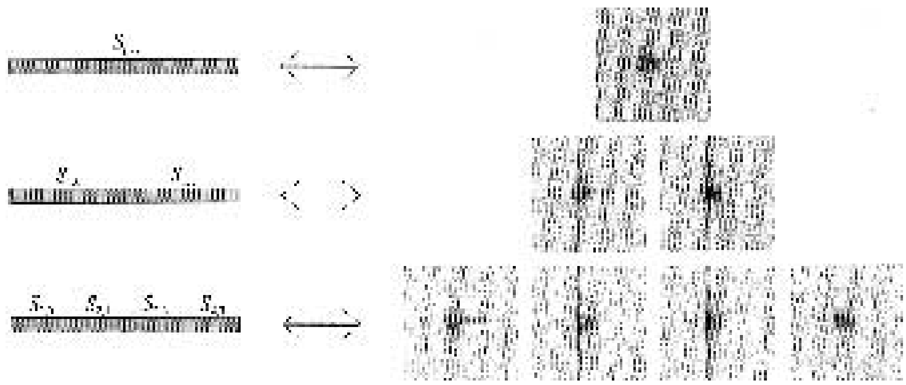

Figure 4. Left: Disjoint half-aperture pyramid. Right: Corresponding sub-aperture images of a BMP-2 at a 17° elevation and 0° azimuth. For each image, the front of the vehicle is the portion nearest the left edge of the image.

captured in this representation. To see this point, note that for all sub-apertures which reside within the main-lobe of the response, the reflectivity estimates are consistently large. As the sub-aperture is expanded, however, the additional signal energy received is relatively insignificant thereby lowering the reflectivity estimate which is normalized with respect to sub-aperture length. Not only does using an excessively large sub-aperture lower the normalized reflectivity estimate, but it also results in a noisier estimate because the additional portion of the aperture being incorporated is dominated by noise[6]. To illustrate that this anisotropic phenomena is clearly present in real data, we show in Figure 4 a three level, disjoint, half-aperture pyramid and the corresponding sub-aperture images for a BMP-2 from the MSTAR public release dataset [6] which uses a 2.8° aperture. Even in this narrow aperture setting, we clearly see that the response associated with the middle section of the aperture contains the majority of the energy from the large scatterer at the front of the vehicle.

3. Anisotropic Scattering Models

Having presented the sub-aperture pyramid, we now proceed to formulate our hypothesis testing problem for anisotropy where the hypotheses are formulated over the sub-aperture pyramid. Our goal is to use the sub-aperture pyramid to develop a general characterization of anisotropy that is not overly-sensitive to azimuthal dependencies such as those produced by geometric scatterers with non-canonical deviations. In particular, we only intend to measure the concentration of unimodal azimuthal scattering and are not concerned with the minor deviations in the azimuthal response that occur with slight changes in scatterer geometry. Two models are presented here that yield this characterization. The first is a simple isolated scatterer model with an intuitive sufficient statistic. This test, however, is susceptible to the interference from neighboring scatterers. This shortcoming motivates the second model which explicitly accounts for the effects of neighboring scatterers. The tests presented in this section are for a fixed scattering location which we assume to be specified. These locations could come from a peak extraction process (for peak attribution as is done in Section 4) or a pre-specified grid (for an image of anisotropy).

3.1. Isolated Scatterer Model

For each sub-aperture $S_{m,i}$, we define an associated scattering hypothesis $H_{m,i}$ over the aperture t via

$$H_{m,i} : a(t) = A 1_{S_{m,i}}(t) \tag{2}$$

where $1_{S_{m,i}}(\cdot)$ denotes the indicator function over $S_{m,i}$ and A is the unknown scattering amplitude of the signal. Thus, each hypothesis corresponds to a scattering response that is uniform over the sub-aperture in question and zero elsewhere. Clearly, this model is an idealization of anisotropic scattering, but because we are only interested in obtaining a general characterization of anisotropy, this model serves our purposes. The set of all possible hypotheses associated with the sub-aperture pyramid is denoted as $\mathcal{H}$.

A reasonable choice of features to test these hypotheses would be all the measured sub-aperture reflectivities $\{q_{m,i}\}$. From the definition of the $q_{m,i}$ in Eq. (1) and partition property (B), it is sufficient to consider the vector $\boldsymbol{q}_M$ of measurements from the smallest sub-apertures since any sub-aperture reflectivity $q_{m,i}$ can be computed from $\boldsymbol{q}_M$ by summing all the $q_{M,j}$ for which the associated $S_{M,j}$ form a partition of $S_{m,i}$, i.e.

$$q_{m,i} = \sum_{j | S_{M,j} \in \mathcal{P}(m,i)} q_{M,j}.$$

As an example, for the three level, half-overlapping, half-aperture pyramid in Figure 2, $q_{1,1} = q_{2,2} + q_{2,4}$ since $S_{2,2}$ and $S_{2,4}$ form a disjoint union of $S_{1,1}$, i.e. $S_{1,1} = S_{2,2} \cup S_{2,4}$ and $S_{2,2} \cap S_{2,4} = \emptyset$. Because $\boldsymbol{q}_M$ is a sufficient statistic for our sub-aperture reflectivities, we take it as our feature vector. The value of this feature vector under hypothesis $H_{m,i}$ and $A = 1$ is denoted as $\boldsymbol{b}(m, i)$ whose j^{th} element is given by

$$\begin{aligned} b(m,i)_j &= \int_{S_{M,j}} 1_{S_{m,i}}(t)dt \\ &= \lambda(S_{M,j} \cap S_{m,i}), \end{aligned} \tag{3}$$

i.e. $b(m, i)_j$ is the portion of the response $1_{S_{m,i}}(t)$ one expects to see over the j^{th} sub-aperture at scale M. We now define our scattering model conditioned on anisotropy hypothesis $H_{m,i}$ as the signal plus noise model

$$q_{M,j} = \int_{S_{M,j}} A 1_{S_{m,i}}(t) + \eta(t)\, dt, \tag{4}$$

where $\eta(t)$ is circularly complex white Gaussian noise with spectral density $2\sigma^2$. This characterization leads to the model

$$H_{m,i} : \boldsymbol{q}_M = A\boldsymbol{b}(m,i) + \boldsymbol{\varepsilon}, \quad \text{with } \boldsymbol{\varepsilon} \sim \mathcal{N}(\mathbf{0}, 2\sigma^2\Lambda), \tag{5}$$

where Λ is the noise covariance structure inherited from the sub-aperture pyramid. The noise in the measured reflectivities in Eq. (5) are characterized as zero-mean circularly complex Gaussians with covariances dictated by the amount of sub-aperture overlap. The elements of the covariance matrix Λ are thus given by $[\Lambda]_{i,j} = \lambda(S_{M,i} \cap S_{M,j})$, which for the half-overlapping half-aperture pyramid in Figure 2 is

$$\Lambda = \frac{1}{2^M} \begin{bmatrix} 1 & .5 & & 0 \\ .5 & \ddots & \ddots & \\ & \ddots & \ddots & .5 \\ 0 & & .5 & 1 \end{bmatrix}.$$

To classify the anisotropy of a scatterer from our vector of sub-aperture measurements $\boldsymbol{q}_M$, we apply a log-likelihood ratio test to the model in Eq. (5) where each log-likelihood is compared to the full-aperture hypothesis $H_{0,0}$. Because there is the unknown reflectivity parameter A, we use a generalized log-likelihood ratio (GLLR) test where for each hypothesis, we take A to be the maximum likelihood (ML) estimate under that hypothesis. For $H_{m,i}$, the matched-filter gives the ML estimate as $\hat{A} = q_{m,i}/L_{m,i}$. Using this estimate results in the GLLR

$$\ell_{m,i} = \frac{1}{4\sigma^2}\left[\frac{1}{L_{m,i}}|q_{m,i}|^2 - |q_{0,0}|^2\right]. \tag{6}$$

Thus, the most likely sub-aperture in this case is the one whose average energy is largest. We note the similarity here to the approach taken by Chaney et al. [2] in which they replace, within the image, the standard full-aperture reflectivity estimate with the maximum sub-aperture reflectivity estimate $|q_{m,i}/L_{m,i}|$, thus using normalized reflectivity (instead of normalized energy) as their criterion for choosing anisotropy. Their approach however is based on intuitive arguments and not a derived statistic. Although this difference may be seemingly small, the effect is quite significant. In particular, using normalized reflectivity, instead of energy, over-compensates for decreasing aperture size. This over-compensation biases their test to choose smaller sub-aperture hypotheses and thus produces images with an excessively coarse imaging resolution. Furthermore, their technique does not address the very significant effect of neighboring scatterers that we discuss next. Thus, when used for image formation, our technique better preserves the fine

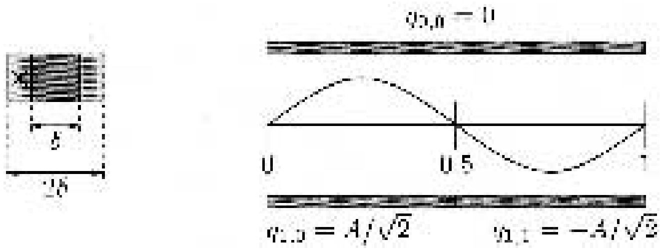

Figure 5. Illustration of how a scatterer that is not in the finest resolution cell can produce a false anisotropy classification from Eq. (6).

resolution of the imagery, where appropriate, since the technique produces more accurate anisotropy classifications.

Though simple and intuitive, the GLLR in Eq. (6) is susceptible to the effects of close proximity neighboring scatterers which are not accounted for in our model in Eq. (4). Recall that the images formed by the smaller sub-apertures have a coarser imaging resolution, and thus the hypotheses are not all consistent in terms of the resolution cell contents. In particular, if a scatterer were located outside the finest resolution cell but within a coarser resolution cell, then the finest resolution reflectivity $q_{0,0}$ would be 0, but $q_{m,i}$ would be large if the resolution cell associated with scale m included the scatterer. We illustrate this point with the example shown in Figure 5. Here a scatterer with amplitude A is located outside the finest resolution cell of size δ but is contained within the coarser resolution cell of size 2δ associated with half-aperture estimates. If this scatterer is isotropic, then the response is the complex exponential illustrated. Integrating over the full aperture gives a 0 reflectivity estimate as expected, but integrating over a half aperture produces a reflectivity with magnitude $A/\sqrt{2}$. Eq. (6) would then classify the center of the resolution cell as anisotropic, even though no scatterer is present in the finest resolution cell.

The problem above is a consequence of not modeling the influence of neighboring scatterers. One of the ways in which the neighboring scatterer manifests itself is through the corruption of the estimated reflectivity as the size of the resolution cell varies. Instead of choosing the ML estimate $\hat{A} = q_{m,i}/L_{m,i}$ as the unknown reflectivity, we can choose the best reflectivity estimate constrained to lie in the finest resolution cell associated with the full-aperture estimate $q_{0,0}$. Choosing $\hat{A} = q_{0,0}/L_{m,i}$ (where the normalization by $L_{m,i}$ accounts for the fact that the modeled azimuthal response is concentrated in a sub-aperture) for all hypotheses can be shown to produce the GLLR statistic

$$\ell_{m,i} = \frac{1}{4\sigma^2}\left[\frac{1}{L_{m,i}}\,|q_{m,i}|^2 - \frac{1}{L_{m,i}}\,|q_{0,0} - q_{m,i}|^2 - \frac{1}{L_{0,0}}\,|q_{0,0}|^2\right]. \tag{7}$$

This statistic is identical to that in Eq. (6) except for the extra term comparing the reflectivity estimates $q_{0,0}$ and $q_{m,i}$. Recall that Eq. (6) compared the average energy in a

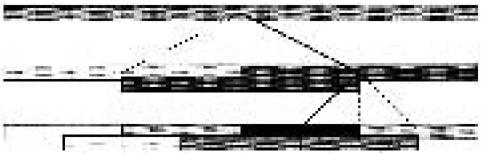

Figure 6. Illustration of how the anisotropy testing can be done in a decision-directed fashion by starting with the largest aperture and at each scale, inspecting only the children of the most likely sub-aperture. Darker shading of the sub-apertures indicate higher likelihoods. Dashed lines denote which hypotheses are tested, and solid lines denote the branch traversed.

sub-aperture to the full-aperture. This new GLLR accounts for the average energy outside the hypothesized sub-aperture as well. Viewed differently, under hypothesis $H_{m,i}$ and our scattering model in Eq. (4)–(5), the values of $q_{0,0}$ and $q_{m,i}$ should simply be noisy perturbations of each other. The new term penalizes when this is not the case thereby enforcing a consistency of the resolution cell contents. Under the example in Figure 5, since the the contribution of each of the half-apertures would be the same, the GLLR is equal to zero for all hypotheses, which is reasonable, since there is no underlying scattering at the focused location.

3.2. *Multiple Scatterer Model*

The modification in Eq. (7) addresses the problem when a neighboring scatterer is isotropic, however, when the neighboring scatterer is anisotropic, problems such as that illustrated by the example in Figure 5 can still arise as the contribution from the interfering scatterer will not integrate out over the full-aperture estimate. To account for this phenomenon, we generalize the model in Eq. (4) to explicitly include multiple scatterers. In particular, we consider the possibility of regularly spaced neighboring scatterers (each with its own anisotropy hypothesis) and incorporate their effects into the anisotropy test. Doing so, we obtain the GLL statistic[7]

$$\ell = \frac{1}{2\sigma^2} \boldsymbol{q}_M' \left[\Lambda^{-1} - 2\Lambda^{-1} BP + P' B' \Lambda^{-1} BP \right] \boldsymbol{q}_M \tag{8}$$

where B and P are defined in Eqs. (14) and (15) of Appendix A. We note that the hypothesis enters into Eq. (8) only via B and P, and thus, the weighting matrix in the brackets is data independent and can be precomputed allowing for a computationally simple GLL that corresponds to a norm on $\boldsymbol{q}_M$.

3.3. *Telescopic Testing*

The sub-aperture pyramid which we use to form our measurements and base our hypotheses is convenient not only for providing anisotropy information, but also for providing an efficient means of performing the hypothesis tests. We can obtain an efficient approximation to the test by evaluating only a small subset of the candidate hypotheses. Due to the nested structure of the sub-apertures (condition (C) in Section 2), we can perform the tests in a telescopic fashion by traversing down a branch in the tree of sub-apertures as depicted in Figure 6. On the pyramid, we expect the likelihoods to increase as the hypothesized sub-apertures "shrink down to" the correct sub-aperture, and then to decrease as the hypothesized sub-apertures "shrink beyond" the correct sub-aperture. This intuition motivates performing the hypothesis test in the following manner:

Step 1. Start with the set of largest sub-aperture(s) at scale $m = 0$. Find the most likely hypothesis at that scale and denote this hypothesis as H_{0,i_0^*}.
Step 2. Consider those hypotheses at scale $m+1$ for which $S_{m+1,i_{m+1}} \subset S_{m,i_m^*}$. Find the one which has the highest likelihood and denote this hypothesis as H_{m+1,i_{m+1}^*}.
Step 3. If the parent is more likely (i.e. $\ell_{m,i_m^*} > \ell_{m+1,i_{m+1}^*}$), then stop and return H_{m,i_m^*} as the estimated hypothesis.
Step 4. If $m+1 = M$, we are at the bottom of the tree, so stop and return H_{m+1,i_{m+1}^*} as the estimated hypothesis. Otherwise, increment m and goto step 2.

This procedure provides an efficient approximation to finding the ML hypothesis without evaluating all the likelihoods. If $H_{m,i}$ is the hypothesis with the highest likelihood, then all that is required for it to be chosen by this scheme is that:

(D) At each scale $n < m$, the sub-aperture at scale n with the highest likelihood is an ancestor of $S_{m,i}$.
(E) The sequence of likelihoods increases as the branch is traversed until $S_{m,i}$ is reached.

Intuitively, these are reasonable conditions that one would usually expect to hold given the interpretation that our tests measure average energy over a sub-aperture. This intuition can be justified under the isolated scattering models. In particular, consider the expected value of $\ell_{n,j}$ when the true hypothesis is $H_{m,i}$ and the proportion of overlap between $S_{n,j}$ and $S_{m,i}$ is given by $\alpha = \frac{\lambda(S_{n,j} \cap S_{m,i})}{\lambda(S_{m,i})}$. For Eq. (6), in which the estimate $\hat{A} = q_{m,j}$ is used, the expected value of the GLLR is

$$\begin{aligned}
\mathbb{E}\left[\ell_{n,j} \mid H_{m,i}\right] &= \mathbb{E}\left[\frac{1}{L_{n,j}} |q_{n,j}|^2 - |q_{0,0}|^2 \middle| H_{m,i}\right] \\
&= \left(\frac{\alpha^2}{L_{n,j}} - 1\right) |A|^2 + (2L_{n,j} + 1)\sigma^2 \\
&\approx \left(\frac{\alpha^2}{L_{n,j}} - 1\right) |A|^2 \qquad (9)
\end{aligned}$$

where the approximation is for high SNR scattering. From this equation, we see the intuitive behavior described above. In particular, to maximize the GLLR at each scale $n < m$, we would choose a sub-aperture that maximizes α (producing $\alpha = 1$) and thus completely overlaps the true sub-aperture, i.e. an ancestor of the true sub-aperture $H_{m,i}$.

Furthermore, for all ancestors of $H_{m,i}$, the expected value of the GLLR increases with decreasing sub-aperture length, i.e. the sequence of expected log-likelihoods increases as the branch is traversed. When the hypothesized sub-aperture becomes too small, the overlap is $\alpha = L_{n,j}/L_{m,i}$, and the expected GLLR decreases. So, as intuition would suggest, the expected value of the GLLR (i) is maximized for the true hypothesis and (ii) obeys conditions (D) and (E) for Eq. (6) under high SNR.

Similarly, for Eq. (7), in which the estimate $\hat{A} = q_{0,0}/L_{m,i}$ is used, the expected value of the GLLR is

$$\begin{aligned}
\mathbb{E}\left[\ell_{n,j} \mid H_{m,i}\right] &= \mathbb{E}\left[\frac{1}{L_{n,j}}|q_{n,j}|^2 - \frac{1}{L_{n,j}}|q_{0,0} - q_{n,j}|^2 - |q_{0,0}|^2 \,\middle|\, H_{m,i}\right] \\
&= \left(\frac{2\alpha - 1}{L_{n,j}} - 1\right)|A|^2 - \left(\frac{1}{L_{n,j}} - 1\right)2\sigma^2 \\
&\approx \left(\frac{2\alpha - 1}{L_{n,j}} - 1\right)|A|^2 \qquad (10)
\end{aligned}$$

where the approximation is for high SNR scattering. The behavior with respect to α and $L_{n,j}$ follow the same trend as for Eq. (9) and thus again supports our intuition for using the telescopic testing. Because of the difficult form of our regularized multiple scatterer log-likelihood given in Eq. (16), we have not shown that the same pattern holds for this extended test, however, intuition and the success demonstrated in the empirical results of Section 4 lead us to believe this behavior holds here as well.

Besides computational efficiency, performing the hypothesis tests in a telescopic fashion also enforces a form of consistency in the sub-apertures tested. In particular, in order for a specific sub-aperture to be chosen, its ancestor hypotheses have to be chosen in the testing at the previous scales. Enforcing such a progression of likelihoods protects against anomalies where a small sub-aperture could possess a high GLLR while none of its ancestors do, such as in the example associated with Figure 5.

3.4. Boxcar Model Deviations

The boxcar hypotheses defined in Eq. (2) are simplified models to which real scatterers do not exactly correspond. One may question whether deviations from this model may drastically effect our hypothesis tests. For example, if the scattering has a sinc($\cdot$) like dependence in azimuth, then the sidelobes[8] will have a large response for a strong scatter and may not be well modeled as additive in the measurement noise ε. To address this issue, we incorporate deviations from the boxcar response into our model. In particular, we start by assuming the underlying *normalized* scattering pattern has been perturbed by white Gaussian noise. For the isolated scatterer model, this modification changes the model response in Eq. (3) to

$$\tilde{b}(m,i)_j = \int_{S_{M,j}} 1_{S_{m,i}}(t) + \nu(t)\, dt$$

where $\nu(t)$ is a circularly complex white Gaussian process with spectral density $2\rho^2$ and is independent of the measurement noise $\eta(t)$. Thus, our modeled measurement vector is now a random vector characterized as

$$\tilde{\boldsymbol{b}}(m,i) \sim \mathcal{N}(\boldsymbol{b}(m,i), 2\rho^2\Lambda).$$

The resulting measurement model is then

$$H_{m,i} : \boldsymbol{q}_M = A\boldsymbol{b}(m,i) + w, \text{ with } w \sim \mathcal{N}(\mathbf{0}, 2(|A|^2\rho^2 + \sigma^2)\Lambda).$$

Thus, we have essentially the same model as in Eq. (5) except that the variance of the noise now depends affinely on the square-magnitude of the underlying scatterer. For consistency, the full-aperture reflectivity estimate is used as the estimate of A in the overall noise variance under each hypothesis. Thus, the statistics for all the hypotheses are scaled by the same factor, and the hypothesis that maximizes the likelihood is not changed by the incorporation of this boxcar deviation.

4. Experimental Analysis

In this section, we examine the behavior of the anisotropy characterization developed in the previous section by studying the dependence on anisotropic phenomenology. In particular, the extended test based on the multiple scatterer model (assuming full-aperture interfering scatterers) is used within the telescopic testing procedure[9]. We start our analysis using narrow-aperture data because of its prevalence in the SAR community. Specifically, we use the MSTAR public release data [6] and data synthetically generated according to MSTAR operational parameters, i.e. a 0.32m cross-range resolution (2.8° aperture), 9.6GHz center frequency, and 0.25m range resolution (590MHz bandwidth). We emphasize that our use of MSTAR parameters is to help promote intuitive understanding, and the results can always be scaled with respect to the aperture size for other settings. For our experiments, we use the three level, half-overlapping, half-aperture pyramid[10] depicted in Figure 2. The number of neighboring scatterers considered is set by $K = 6$ and their spacing is set by the MSTAR oversampling rate of $\Delta_r/\Delta_p = 1.25$. The value of the regularization parameter on neighboring reflectivities is set by $\gamma = 0.5$. Deviations from the boxcar model are accounted for by setting $\rho = 0.1$.

To first demonstrate that our test reveals anisotropic behavior in real data, we show in Figure 7 the anisotropy attributions for peaks extracted from a BMP-2 tank at 0°, 30°, 60°, and 90° azimuths and a 17° depression. Each image displays the log-magnitude reflectivities using darker shades to indicate stronger reflectivities. Peak locations and anisotropy characterizations are given by the symbol overlays in each image. A circle denotes a full-aperture classification; a square denotes a half-aperture classification; a triangle denotes a quarter-aperture classification. Even though the aperture associated with

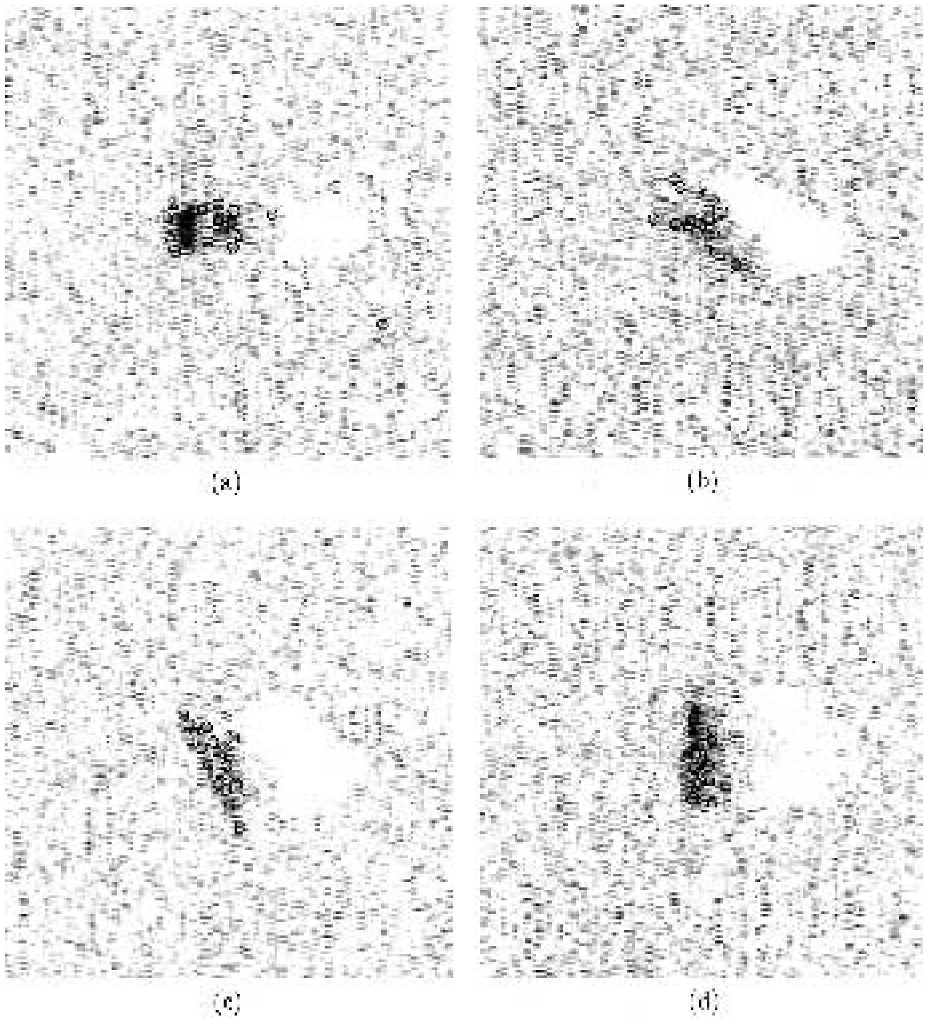

Figure 7. Anisotropy characterization of peaks extractions on a BMP-2 tank at (a) $0°$, (b) $30°$, (c) $60°$, and (d) $90°$ azimuths.

this data set is relatively small at $2.8°$, we note that we are still able to detect anisotropic scattering particularly at cardinal azimuthal orientations.

The images in Figure 7 show that scatterers are being classified as anisotropic; however, the images do not convey how useful that information is in characterizing targets. This topic is addressed by Kim, et al. [7] where anisotropy is used as an attribution in a peak-based Bayes classifier. One of the more interesting results in that work is that scatterer anisotropy is significantly more stable at near-cardinal target orientations than at off-

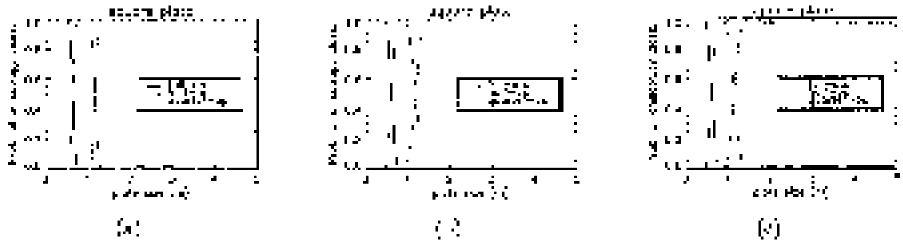

Figure 8. Anisotropy plots for a square plate in Gaussian noise at 20dB PSNR. (a) no azimuthal and location uncertainty; (b) maximal azimuthal uncertainty and no location uncertainty; (c) maximal azimuthal uncertainty and location uncertainty given by peak extraction.

cardinal orientations which argues for at least two distinct sources of anisotropy. In particular, we expect geometric scattering to dominate the near-cardinal orientations and produce consistent anisotropy attributions but volumetric scattering to dominate at off-cardinal orientations and produce erratic anisotropy attributions. To verify this intuition, we separately study our proposed anisotropy characterization for the canonical flat plate and volumetric scatterers using synthesized data. In both cases, we use what we call an anisotropy plot to convey the dependence of our anisotropy classification on an underlying parameter. In the case of the canonical flat plate, this parameter is the plate size, and in the case of the volumetric scatterer, this parameter is the distribution of constituent scatterers.

4.1. Geometric Anisotropy

To examine geometric anisotropy, we synthesize azimuthal data for the flat plate according to the physical optics model using MSTAR parameters. To generate the associated anisotropy plots, we use probability estimates based on Monte Carlo runs involving 8192 trials for each plate size where the scatterer is taken at broadside and white Gaussian noise is added across the aperture. The PSNR of the signal is kept constant at PSNR $=$ 20dB, thus noise variance scales with the maximum peak reflectivity.

The anisotropy plot under these settings is shown in Figure 8(a). Contained in this figure are three curves each of which represents the probability of a particular anisotropy classification conditioned on the size of the scatterer. Thus, the three values for a given plate size represent the PMF of these anisotropy classifications (i.e. full, half, and quarter-aperture) conditioned on that plate size. As expected, the full-aperture classification dominates for the smaller plate sizes. As plate size is increased, the half-aperture classification starts to dominate. Between 0.8m and 1m, the half-aperture classification probability is approximately one. The noiseless azimuthal response for a plate size in the middle of this region (0.9m) is shown in Figure 9(a) which is quite reasonably classified as half-aperture. The solid curve in the figure represents the real component of the response, and the dashed curve represents the imaginary component. The vertical lines are a visual aid dividing the aperture into eighths. As plate size is increased beyond 1m, the classification transitions from half-aperture to quarter-aperture in the anisotropy plot of

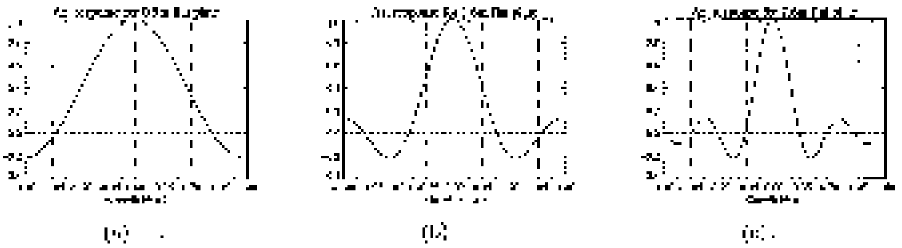

Figure 9. Azimuthal response for different plate sizes: (a) 0.9m, (b) 1.6m, and (c) 2.6m.

Figure 8(a). Between 1.3m and 1.9m, the quarter-aperture classification probability is approximately one. The azimuthal response for a plate size in the middle of this region (1.6m) is shown in Figure 9(b) which also agrees with what one would expect. Intuition would suggest that the probability of anisotropy classification would be unimodal and in particular that the probability of the quarter-aperture classification would be monotonically increasing with plate size (since quarter-aperture anisotropy is the most anisotropic classification available), however, this is not the case. In particular, starting at about 1.9m, the quarter-aperture classification rate begins to decrease. The middle of the range where the rate drops is about at 2.6m. The azimuthal response for this plate size is shown in Figure 9(c). Based on this response, we would expect the scatterer to be classified as quarter-aperture anisotropy. In fact, the null-to-null bandwidth is a quarter of an aperture. So, the question is why is this scatterer occasionally classified as full-aperture scattering. This result is an artifact from the scale-telescopic hypothesis testing. To see this point, observe the GLLR's for the noiseless signal given in the first column of Table 1. From these values, we see that the quarter-aperture hypothesis does in fact produce the highest GLLR, but because the full-aperture hypothesis is nearly as likely as the half-aperture hypothesis, the quarter-aperture hypothesis is not always not tested. To gain a better understanding of why the full-aperture hypothesis is nearly as likely as the half-aperture hypothesis, consider the GLLR for our simple test that does not consider neighboring scatterers, i.e. the one which corresponds to Eq. (7), that compares normalized sub-aperture energies. For the 2.6m plate, the second zero-crossings of the sinc-like azimuthal response are located such that they minimize the reflectivity in the center half-aperture, i.e. the first sidelobes maximally negate the influence of the mainlobe. Thus, the middle half-aperture reflectivity is reduced and produces a correspondingly lower GLLR for this hypothesis. Similarly, the quarter-aperture classification rate "dips" at plate sizes near multiples of 2.6m as the other "negative" sidelobes have a locally maximal negative effect on the middle half-aperture[11]. This problem could easily be alleviated by relaxing the hard decision made at each scale in the telescopic hypothesis test. However, we do not use such a test here because as is discussed next, this problem is not as significant in a more realistic setting that incorporates the presence of azimuthal uncertainty.

The anisotropy plot in Figure 8(a) is for when the plate is oriented exactly broadside to the radar. To incorporate the effects of azimuthal uncertainty, we modify the setup as follows. We generate SAR data with the same parameters as before except that the aperture

Table 1. GLLR's for noiseless 2.6m plate response (assuming an PSNR of 20dB).

	Without azimuthal uncertainty	With azimuthal uncertainty
full-aperture	0	0
half-aperture	0.60	1.0–2.3
quarter-aperture	8.4	4.2–7.5

size is increased by a factor of three, i.e. data is generated over a 8.4° aperture. From this extended aperture, we randomly take a section measuring 2.8° from a uniform distribution whose support is given by the following cases to maximize the azimuthal uncertainty subject to observing the mainlobe response.

- If the plate size is less than two wavelengths (i.e. the plate size is less than 6.25 cm), then the scatterer is considered isotropic and any 2.8° section of the extended aperture can be selected,
- If the plate size is larger than two wavelengths but still small enough such that the half-power bandwidth of the azimuthal response is larger than 2.8°, then any section of the extended aperture within the half-power band can be chosen, and
- If the plate size is sufficiently large such that the half-power bandwidth of the azimuthal response is smaller than 2.8°, then any section of the extended aperture containing the half-power band can be chosen.

The resulting anisotropy plot is shown in Figure 8(b). Interestingly, performance is improved for larger plate sizes by the addition of azimuthal uncertainty. Looking at the GLLR's in the second column of Table 1 for the 2.6m plate (assuming 20dB PSNR), we see that it is *not* that the quarter-aperture likelihood increases (in fact it decreases slightly to typically vary between 4.2 and 7.5) but that the half-aperture likelihood increases to typically vary between 1.0 and 2.3. This GLLR increases because the exact broadside orientation represents a worst-case scenario for the half-aperture hypothesis (relative to the full-aperture hypothesis) due to the maximal negative effect that the first (and other odd number) sidelobes have on the middle half-aperture reflectivity as previously described. Azimuthal uncertainty, however, perturbs this degenerate alignment.

In addition to azimuthal uncertainty, we can also observe the effect of location uncertainty which we simulate by using a peak extraction step[12] to determine the scatterer location. The resulting anisotropy plot is shown in Figure 8(c). Not surprisingly, there is slight degradation in performance, particularly for larger plate sizes. This degradation is due to the fact that large plates span several resolution cells over which their reflectivity is approximately the same. Thus, the peak extraction is susceptible to noise over these resolution cells and frequently reports a location that, while on the scatterer, does not correspond to the scattering center. The resulting peak location error introduces a modulation on the observed azimuthal response which distorts the anisotropy classification. In particular, for larger apertures, the linear phase on the azimuthal response prevents the sub-aperture reflectivity estimates from reaching their true value due to the destructive interference that occurs when integrating over the sub-apertures. Thus, the energy from larger sub-apertures is more heavily biased towards smaller values. Smaller sub-apertures, on the other hand, are less susceptible to this phase variation due to the shorter integration interval and thus give stronger reflectivity estimates. This interference is the reason that errors in scatterer location tend to bias the anisotropy classification towards higher degrees of anisotropy.

The anisotropy plots in Figure 8 show that even in the presence of azimuthal and location uncertainty, our anisotropy measure exhibits the strong dependence of anisotropy on plate size that is predicted by canonical scattering models. Furthermore, we see that the anisotropy classifications are consistent with these models as illustrated in Figure 9. One would naturally expect the dependencies in the anisotropy plot to be preserved as the aperture size is increased. As we discuss in Section 4.3, this is in fact true, but this seemingly trivial property turns out to be quite significant when contrasted to the behavior of volumetric anisotropy which we discuss next.

4.2. Volumetric Anisotropy

Similar to the anisotropy plots for the flat plate scatterer, we generate anisotropy plots for volumetric scatterers where the dependent variable corresponds to the "size" of the scatterer which in this case is the spatial support of the pdf generating the individual isotropic scatterers. The radar and sub-aperture parameters are the same as those used for the geometric anisotropy plots. For each Monte Carlo sample, a volumetric scatterer is taken as a collection of random point scatterers generated according to the following parameters:

- The density of the scatterers in terms of the average number of scatterers per resolution cell.
- The mean and variance of the normal distribution producing the real-valued reflectivity of the scatterers. Both of these values have been set to 1, and the distribution is truncated to prevent negative values.
- The support for the uniform distribution producing the down-range and cross-range location of the scatterers. The support of the pdf producing the down-range location of the scatterers is taken as one resolution cell. The support of the pdf producing the cross-range location is the dependent variable in the anisotropy plot.
- The azimuthal uncertainty which is produced using a uniform pdf with a support of $[-0.7^\circ, 0.7^\circ]$, i.e. shifts up to a quarter of the aperture are allowed.
- The PSNR of the collective scattering which is taken to be 20dB.

In Figure 10, we show the anisotropy plots for scattering densities of 1, 10, and 100 scatterers per resolution cell or equivalently 0.32, 3.2, and 32 scatterers per meter in cross-range under a 2.8° aperture. From these plots, it is immediately clear that the behavior of volumetric anisotropy is heavily dependent on the spatial density of the constituent scatterers. In particular, the plots go from saying that anisotropy is independent of size for low scattering densities to saying that anisotropy is highly dependent on

Figure 10. Anisotropy plots for volumetric scatterers with scattering density of (a) 1, (b) 10, and (c) 100 scatterers per resolution cell.

the size at densities sufficiently high that the aggregation resembles a flat plate. The behavior in these plots is quite reasonable. For an average of one scatterer per resolution cell, we would expect the model to usually be able to separate the individual isotropic scatterers, thus producing the full-aperture classification. However, this is not always the case because scatterers may occasionally be considerably closer than one resolution cell apart or the peak extraction may cause the algorithm to focus to the wrong location. For a scattering density of 100 scatterers per resolution cell, there are so many scatterers drawn from the uniform distribution that the aggregation very closely resembles a flat plate of the same size as the support. Deviations from the anisotropy plot for the flat plate can be attributed to

1. the scatterers are not regularly spaced since their locations are random and
2. the amplitudes on the scatterers are random.

The anisotropy plot for a density of 10 scatterers per resolution cell is a transitional phase between the two extreme cases of one and 100 scatterers per resolution cell.

From the anisotropy plots in Figure 10, we conclude that low density volumetric scattering is preferable to high density scattering because the former has a lower incidence of volumetric anisotropy attributions. This effect allows for anisotropic classifications to be more confidently associated with geometric scatterers from which reliable information can be inferred. One may at first be inclined to believe that the density of volumetric scattering is a physical parameter over which we have no control, but this is not the case. The scattering density in our analysis is with respect to the number of scatterers per resolution cell, and the size of the resolution cell is inversely related to the size of the aperture. Thus, by using wide-aperture data, we should be able to reduce volumetric scattering density and hence the detection rate for volumetric anisotropy as discussed in the next section.

4.3. Extension to Wide-Aperture Data

The results in Figures 8 and 10 are promising in that they imply that by increasing the size of the aperture, one can preserve the detection rate for geometric anisotropy classifications while reducing the rate of volumetric anisotropy classifications. This effect allows for a devoted analysis of predictable anisotropic geometric scatterers in an ATR algorithm.

For low density volumetric scattering (per resolution cell), Figure 10 shows that the anisotropy classification is usually full-aperture regardless of the cross-range support. However, at medium to high scattering densities, the number of anisotropy classifications increase. Wide-aperture data should thus reduce the number of anisotropy classifications because increasing the length of the aperture reduces the scattering density in terms of the number of scatterers per resolution cell. For example, increasing the aperture size by a factor of ten decreases the resolution cell size and hence scattering density by the same factor. From the anisotropy plots, we see that such a factor should have a significant impact on volumetric anisotropy classification. Geometric scatterers, however, can be considered to be composed of a continuum of infinitely small scatterers (with respect to practical imaging resolutions), so increasing the resolution by an order of magnitude does not detract from the high scatterer density thus preserving the structure of the anisotropy plot.

The above is an image (or spatial) domain motivation for why wide-aperture data would reduce the rate of volumetric anisotropy while preserving the rate of geometric anisotropy, but there is also an azimuthal domain interpretation. Consider a scatterer which is declared anisotropic based on narrow-aperture data. This classification is made because most of the energy is concentrated in one region of the aperture. When the size of the available aperture is increased for volumetric scatterers, there is likely to be a considerable amount of energy in the newly appended sub-apertures because (as depicted in Figure 1(b)) the underlying response is not truly unimodal. However, geometric scatterers with a unimodal azimuthal response should have little energy in the appended sub-apertures. Furthermore, many anisotropic geometric scatterers exhibit sinc-like oscillations in the appended sub-apertures (which nearly integrate to zero) while many volumetric scatterers do not. Thus, for volumetric scatterers there is likely to be considerable energy in newly appended sub-apertures which may change the anisotropy classification, but this is not the case for geometric scatterers.

To verify this conjecture empirically, we generate anisotropy plots for the geometric and volumetric scatterers in the same fashion as before except that the aperture size is increased by a factor of eight. This modification naturally changes the sub-aperture pyramid we use. To be consistent with the narrow-aperture results, we use a three level, half-overlapping, half-aperture pyramid[13] which consists of 1/8 apertures at scale 0, 1/16 apertures at scale 1, and 1/32 apertures at scale 2. These hypotheses correspond to the full, half, and quarter-apertures in the narrow-aperture case and are thus consistent in terms of the physical size of the underlying scatterer. To prevent any confusion between the wide and narrow-aperture cases, we will refer to these hypotheses with their measurements in degrees, i.e. 2.8°, 1.4°, and 0.7°. To be consistent in the geometric and volumetric settings, azimuthal uncertainty in both cases is modeled with a uniform distribution over 1/4 of the narrow-aperture, i.e. 0.7°. For consistency in the noise level between the narrow and wide-aperture settings, we use the same noise spectral density (in the azimuthal domain) as in the narrow-aperture case. Thus, for isotropic scatterers, the wide-aperture PSNR is actually higher than in the narrow-aperture case, and for anisotropic scatterers, the PSNR is lower due to the coherent averaging involved.

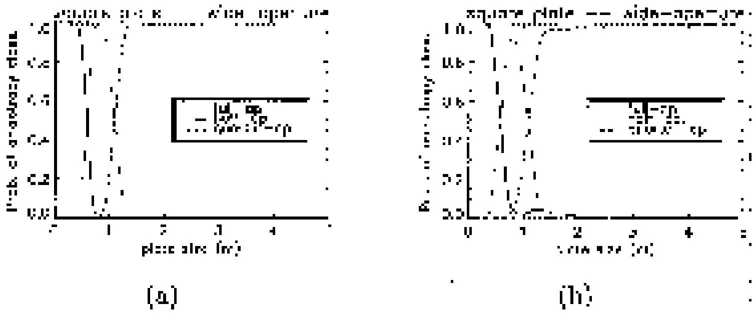

Figure 11. Anisotropy plots for the canonical flat plate scatterer using (a) coarse-resolution peak extraction and (b) high-resolution peak extraction.

The wide-aperture geometric anisotropy plot is displayed in Figure 11. The two plots in Figure 11 correspond to two different peak extraction methods. Figure 11(a) is for coarse-resolution peak extraction which is done using the center 2.8° narrow-aperture. Figure 11(b) is for high-resolution peak extraction which is done using the full-aperture. As predicted, Figure 11(a) looks quite similar to the narrow-aperture anisotropy plot in Figure 8(c) showing a strong dependence on the underlying plate size. Figure 11(b) also looks similar to Figure 8(c), but the classification rates for 1.4° and 0.7° anisotropy have unexpectedly dropped for larger plate sizes. One can also see that the “transition band” between anisotropy classifications is wider for the high-resolution peak extraction. This effect is due to the fact that in the high-resolution setting, the plate sizes corresponding to the degrees of anisotropy that we are testing span several resolution cells. Over these resolution cells, the reflectivity is nearly constant resulting in a peak location which comes from a uniform distribution over the size of the scatterer. The resulting location error for the scattering center induces a modulation over the azimuthal response which distorts the anisotropy classification as discussed in Section 4.1. This problem is not significant for the coarse-resolution peak extraction because the coarse-resolution cell size is the same order of magnitude as the plate sizes. Thus, the spatial averaging usually covers a significant portion of the scatterer and is more likely to return a peak location near the center of the flat plate.

We now consider the behavior of volumetric scatterers in the wide-aperture setting. The nominal scattering density that we examine is 10 scatterers per coarse-resolution cell or equivalently 1.25 scatterers per resolution cell in the high-resolution setting. Figure 12 displays the wide-aperture anisotropy plots. Figure 12(a) is for the coarse-resolution peak extraction using the center 2.8° narrow-aperture, and Figure 12(b) is for the high-resolution peak extraction using the full-aperture. The volumetric anisotropy plot in Figure 12(b) behaves as conjectured, bearing a close resemblance to the anisotropy plot for a scattering density of one scatterer per resolution cell in the narrow-aperture setting. However, Figure 12(a) shows virtually no reduction in the rate of anisotropy classifications. Recalling the image domain rationale that wide-aperture data reduces volumetric anisotropy because we are better able to resolve constituent scatterers, this result is not

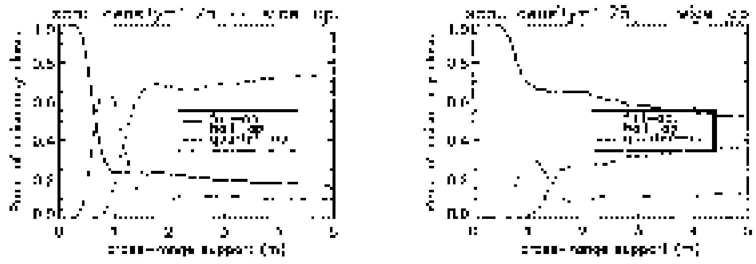

(a) (b)

Figure 12. Anisotropy plots for volumetric scatterers with scattering density of 10 scatterers per coarse-resolution cell using (a) coarse-resolution peak extraction and (b) high-resolution peak extraction.

surprising. When we use the coarse-resolution peak extraction, we are not focusing on peaks that could be resolved in the high-resolution regime thus disregarding that information which would benefit us.

The dependence on the peak extraction process can be summarized by saying that the coarse-resolution peak extraction preserves the anisotropy classification rates for both geometric and volumetric scatterers, while high-resolution peak extraction preserves the classification rate for geometric scatterers to a lesser degree but significantly reduces the rate for volumetric scatterers. However, by combining the coarse and high-resolution peak extractions, we should be able to obtain the desired behavior for both geometric and volumetric anisotropy. In particular, we can select which peak extraction method to use based on scatterer size inferred from the anisotropy attribution. Recall that the high-resolution peak extraction degrades the geometric anisotropy plot because the extraction provides a worse peak location estimate for larger plate sizes which causes the degree of anisotropy to be over-estimated. Because this effect only occurs for larger plate sizes and higher degrees of anisotropy are associated with larger scatterers, we know that in this situation, it can only be beneficial to repeat the anisotropy attribution of the scatterer using the coarse-resolution peak location which gives a more accurate estimate of the scattering center. Thus, we first use the peak location from the high-resolution peak extraction, and if the extraction is declared anisotropic (conveying that there is likely to be a large geometric scatterer there), then we defer to the peak location from the coarse-resolution peak extraction and use its associated anisotropy classification[14]. Thus, using this approach, the high rate of minimally anisotropic 2.8° classifications is preserved for volumetric scatterers since they do not defer to the coarse-resolution peak extraction. The 1.4° and 0.7° classifications for geometric scatterers, however, are also largely preserved since their initial anisotropy classification is usually over-estimated and thus defers to the location estimate given by the coarse-resolution peak extraction.

The anisotropy plots using this combination of coarse and high-resolution peak extractions are given in Figure 13. Not surprisingly, this approach is not better than using coarse-resolution for the geometric scatterers nor better than only using the high-resolution for the volumetric scatterers, but this technique offers a good trade-off resulting in an

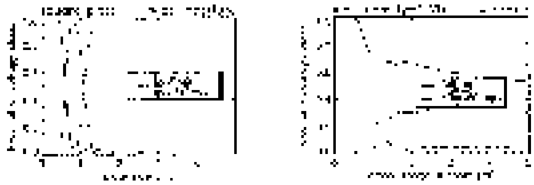

(a) (b)

Figure 13. Anisotropy plots using both the high and coarse-resolution peak extractions for the (a) geometric flat plate scatterer and (b) volumetric scatterer with 10 scatterers per coarse-resolution cell.

algorithm which works well on both geometric and volumetric scatterers. Thus, as the reasoning at the beginning of this section implied, by using wide-aperture data, we can significantly reduce the rate of volumetric anisotropy while preserving the rate of geometric anisotropy.

Up to now, for clarity in the comparison of narrow and wide-aperture anisotropy attributions, we have use the same hypothesis set of {2.8°, 1.4°, 0.7°} sub-apertures (which we call the *restricted hypothesis set*) for both cases. However, in addition to reducing the rate of volumetric anisotropy (while preserving that of geometric anisotropy), wide-aperture data allows for additional anisotropy hypotheses up to the size of the larger aperture. These additional anisotropy hypotheses do not effect the argument for reducing the rate of volumetric anisotropy, however, they does allow for a more refined anisotropy characterization of smaller scatterers by the corresponding additional degrees of anisotropy. To demonstrate this point, we show in Figure 14 the geometric anisotropy plots for the flat plate scatterer with the *augmented hypothesis set* of {22.5°, 11.3°, 5.6°, 2.8°, 1.4°, 0.7°} sub-apertures from the half-overlapping, half-aperture pyramid. The domain of plate sizes here is reduced to 0m−2.5m to better illustrate the behavior for small scatterers. The behavior exhibited is a natural extension of the geometric anisotropy plots in Figures 11 and 13(a). In particular, the only significant effect is for the 2.8° classification which is the

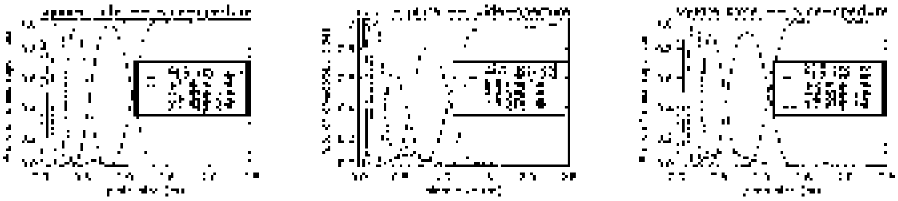

(a) (b) (c)

Figure 14. Anisotropy plots for the canonical flat plate scatterer using the augmented hypothesis set and (a) coarse-resolution peak extraction, (b) high-resolution peak extraction, (c) combination of coarse and high-resolution peak extractions.

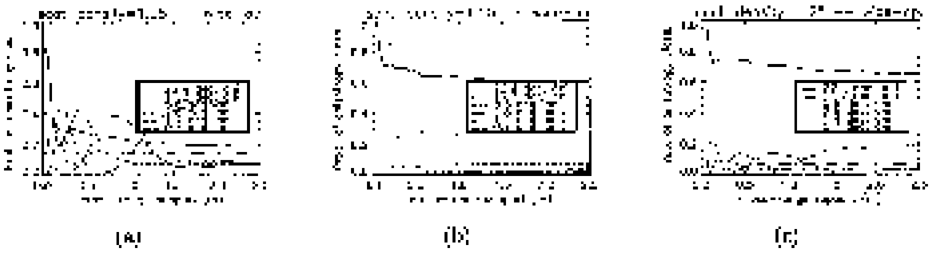

Figure 15. Anisotropy plots for volumetric scatterers with scattering density of 10 scatterers per coarse-resolution cell using the augmented hypothesis set and (a) coarse-resolution peak extraction (b) high-resolution peak extraction (c) combination of coarse and high-resolution peak extractions.

least anisotropic classification in the restricted hypothesis set. Under the new augmented hypothesis set, scatterers which were previously characterized as 2.8° are now classified as 22.5°, 11.3°, 5.6°, or 2.8°. The 22.5° classification dominates the smallest plate sizes, and the dominant attribution transitions to 11.3°, 5.6°, and 2.8° as plate size is increased. Interestingly the 22.5° classification probability starts out noticeably lower for the coarse-resolution peak extraction than for the other two methods. The reason for this error is that for the smaller plate sizes, the coarse-resolution peak extraction introduces location errors on the order of size of the coarse-resolution cell. As previously noted, location error introduces a modulation on the observed azimuthal response which biases the classification result to higher degrees of anisotropy. However, since this location error is small, the only effect is to misclassify some of the small plates as 11.5° instead of 22.5°. Note that in the combined coarse and high-resolution approach, the vast majority of these small plates are characterized as 22.5°. This correct attribution is declared because the anisotropy attribution from the high-resolution peak extraction is analyzed before the coarse-resolution extraction, and thus, the decision is not deferred to the coarse-resolution extraction.

In Figure 15, we show the volumetric anisotropy plots using the augmented hypothesis set. Again, the behavior of each plot is a natural extension of Figures 12 and 13(b). In particular, the coarse-resolution peak extraction shows a high rate of anisotropic classifications, but the high-resolution extraction allows for the scatterers to be frequently resolved into individual isotropic scatterers. The combination of the two methods preserves the separation of interfering scatterers to suppress the rate of volumetric anisotropy.

4.4. Collected Wide-Aperture Data

In this section, we apply our anisotropy attribution to peaks extracted from measured wide-aperture data. The data has a resolution of 1.9 inches in down and cross-range achieved using a 4GHz bandwidth, a 10GHz center frequency, and a 26° aperture. For narrow-aperture comparisons, we take a 3.3° section of this aperture (i.e. 1/8 of the wide-aperture) as our narrow-aperture data. For each narrow-aperture peak extraction, we apply our anisotropy test with the hypothesis set of {3.3°, 1.6°, 0.8°} sub-apertures whose elements correspond to the full, half, and quarter narrow-apertures. For the wide-aperture data, we use the combined coarse and high-resolution peak extraction method described in the previous section. Because the wider aperture allows for more anisotropy hypotheses to be defined, we have several choices for the hypothesis set in this regime. We examine two particular sets. The first is the restricted hypothesis set of {3.3°, 1.6°, 0.8°} sub-apertures used in the narrow-aperture case. The other set is the augmented hypothesis set obtained by taking all the sub-apertures in the half-overlapping, half-aperture pyramid for the wide-aperture. The sub-aperture sizes in the augmented hypothesis set are thus 26°, 13°, 6.5°, 3.3°, 1.6°, and 0.8°. In Figures 16 and 17, we show the log-magnitude imagery at MSTAR resolution[15] with extracted peaks and their associated anisotropy attribution for two different vehicles. The symbol overlays in Figures 16(a) and 17(a) specify the location and anisotropy attribution of each peak extraction based on narrow-aperture data. In these figures, a black circle is used to denote 3.3° anisotropy, a square is used to denote 1.6° anisotropy, and a triangle is used to denote 0.8° anisotropy. The symbol overlays in Figures 16(b) and 17(b) again specify peak location and anisotropy attribution, except they are now based on wide-aperture data. To denote the additional wide-aperture 26°, 13°, and 6.5° hypotheses, we again use a circle, square, and triangle, respectively, but display them in white instead of black.

For each of the vehicles, we see that peak extractions that are labeled as the same (or nearly the same) degree of anisotropy in the narrow and wide-aperture settings can frequently be associated with an apparent geometric scatterer. In particular, we note in Figure 16(b) the collections labeled "A" and "B" appear to be large geometric scatterers

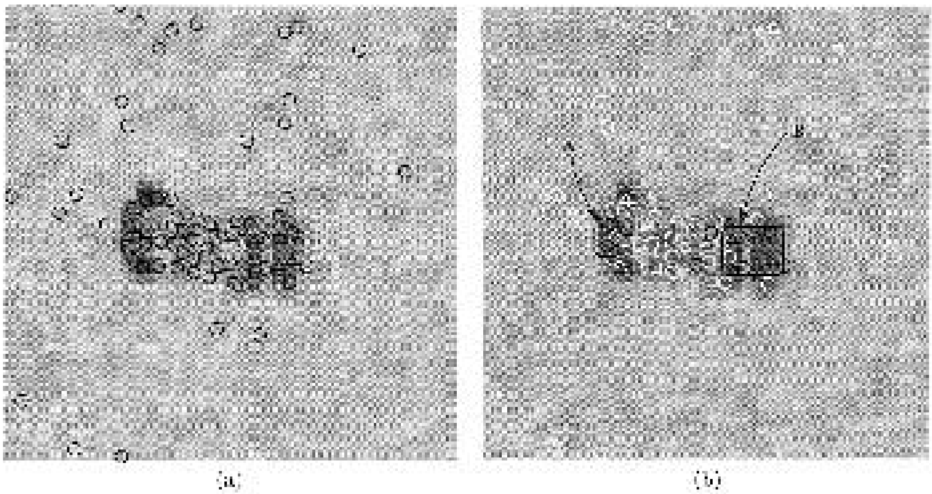

Figure 16. Anisotropy characterization of peaks from wide-aperture data for vehicle 1. (a) Narrow-aperture based anisotropy attributions. (b) Wide-aperture based anisotropy attributions.

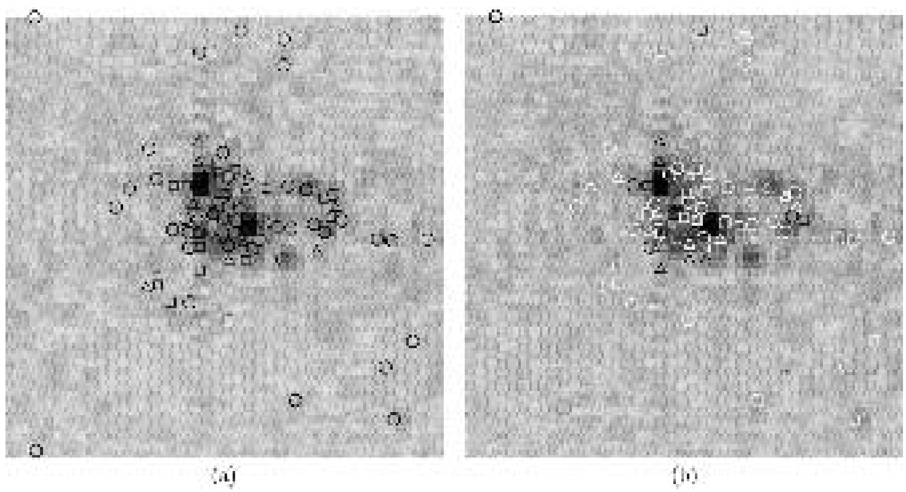

Figure 17. Anisotropy characterization of peaks from wide-aperture data for vehicle 2. (a) Narrow-aperture based anisotropy attributions. (b) Wide-aperture based anisotropy attributions.

at the front and rear of the vehicle and are appropriately characterized as anisotropic. Note that based on the narrow-aperture data, the two scatterers labeled "A" are attributed as 3.3° in Figure 16(a), but there is no means of telling if the underlying scatterers are actually 3.3° or perhaps less anisotropic since 3.3° is the lowest degree of anisotropy available in the narrow-aperture setting. However, with the augmented hypothesis set for wide-aperture data, we see that in fact they are both approximately 3.3°, and not much more. This result demonstrates how the additional hypotheses afforded by the larger aperture allow more anisotropy information to be conveyed for smaller scatterers. We also point out that in Figures 16 and 17, those peak extractions which do not have the same anisotropy attribution in the narrow and wide-aperture regime are frequently not identifiable with a geometric scatterer and have a less anisotropic classification (usually the minimally anisotropic 26° classification) in the wide-aperture setting.

So far, we have observed the conjectured benefit of wide-aperture data over narrow-aperture data on the anisotropy characterization of geometric scatterers, i.e. the preservation of higher degrees of anisotropy in the narrow-aperture data and elaboration of the least anisotropic narrow-aperture hypothesis by augmenting the hypothesis set with larger sub-aperture hypotheses. This result is predicted by the analysis presented earlier. That analysis also predicted a reduction in the rate of volumetric anisotropy as aperture size is increased. To test this behavior with real data, we use the wide-aperture data focused on clutter using 26° and 3.3° apertures as before. In particular, we examine the three clutter scenes composed of trees and field shown in Figure 18 where the narrow-aperture anisotropy characterization is displayed in the left-hand side and the wide-aperture characterization is displayed in the right-hand side. The set of hypotheses and respective graphical labels are the same as in Figures 16 and 17. It is immediately clear that there is a significant

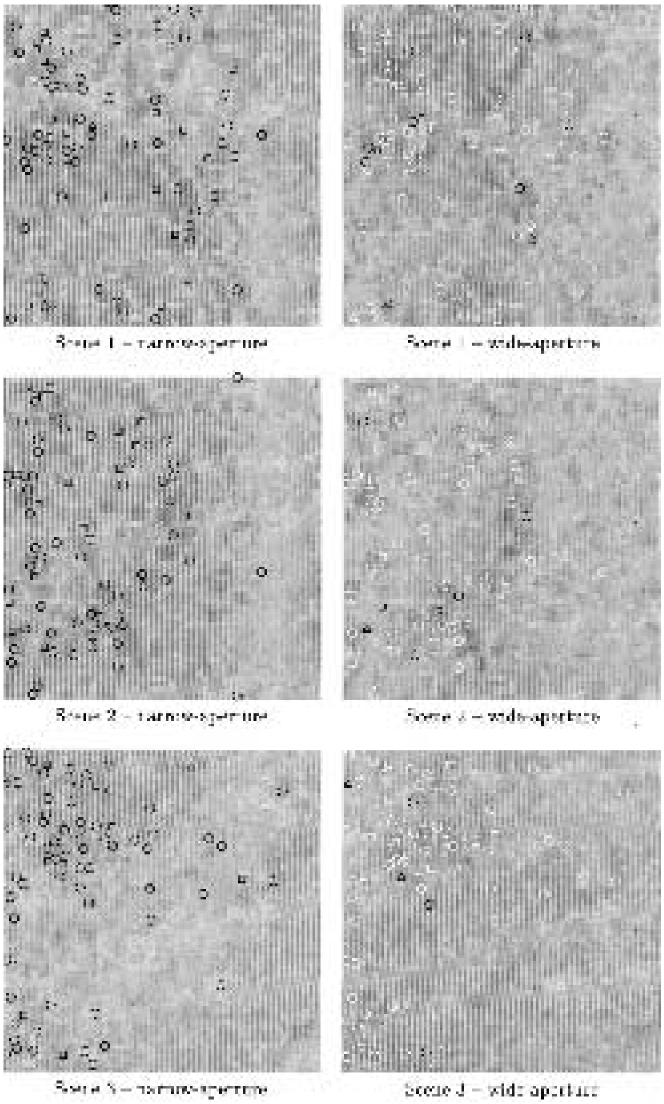

Figure 18. Anisotropy characterization of peaks from 3 instances of clutter in the wide-aperture data. Left: Narrow-aperture anisotropy attributions. Right: Wide-aperture anisotropy attributions.

reduction in the rate of higher degrees of anisotropy using wide-aperture data. To explicitly see that this reduction is due to the volumetric scatterers being resolved into individual isotropic scatterers (in contrast to their simply being independently distributed over the larger hypothesis set), we show in Tables 2 and 3 the tabulated anisotropy correspondences

Table 2. Anisotropy classification correspondences for clutter with narrow and wide-aperture data using the same anisotropy hypotheses.

Narrow-ap.\Wide-ap.	3.3°	1.6°	0.8°
3.3°	176	0	0
1.6°	45	0	1
0.8°	3	0	0

Table 3. Anisotropy classification correspondences for clutter with narrow and wide-aperture data using the augmented hypothesis set for wide-aperture data.

Narrow-ap.\Wide-ap.	26°	13°	6.5°	3.3°	1.6°	0.8°
3.3°	117	28	10	15	3	3
1.6°	29	8	5	2	0	2
0.8°	1	2	0	0	0	0

between the two cases. Table 2 shows the correspondences between the narrow and wide-aperture anisotropy classifications when both are restricted to use the same set of narrow-aperture hypotheses. The empirical results here strongly argue that the wider aperture has resolved the scatterers which were attributed as 1.6° and 0.8° under the narrow-aperture into individual minimally anisotropic 3.3° scatterers. Table 3 shows the same as Table 2 except that the correspondences here are for when the augmented hypothesis set is used for the wide-aperture data. Here we see that many of the 3.3° anisotropy classifications are further resolved into the less anisotropic classifications and the majority of them are assigned to the 26° minimal degree of anisotropy. Thus, we see the predicted reduction in the rate of volumetric anisotropy in real wide-aperture data.

5. Conclusions

We have proposed a general characterization of anisotropy based on concentrated scattering in azimuth. A sub-aperture pyramid is used to generate a tree of multi-resolution images at a variety of cross-range versus azimuthal resolutions allowing for the detection of anisotropic phenomena. With each sub-aperture in the pyramid, we associate a hypothesis that the azimuthal scattering is confined to and uniform over that sub-aperture. This model then leads to a sequence of hypothesis tests to characterize anisotropy which can be approximated with an efficient pruning algorithm due to the tree-structure over the sub-apertures.

This characterization of anisotropy allows us to explore some of the underlying phenomenology behind anisotropic scattering. In particular, we study the canonical flat plate and volumetric scatterer. Anisotropy plots clearly show a strong observability of the inverse relation between plate size and degree of anisotropy that is predicted by physics-based models. Anisotropy is also strongly dependent on the spatial distribution of a dense cluster of isotropic scatterers composing a volumetric scatterer, however, as the density of scatterers is reduced, this dependence decreases as the scatterers are more frequently resolved into constituent isotropic scatterers. The dependence of volumetric anisotropy on the density of the scatterers leads to the attribute that the probability of volumetric anisotropy classifications can be reduced by increasing the size of the aperture. The only significant effect on geometric anisotropy of extending the aperture is related to additional hypotheses (corresponding to larger sub-apertures) in the augmented hypothesis set. In particular, the larger sub-aperture hypotheses allow for a more accurate characterization of smaller scatterers which exhibit broader (but still anisotropic over the wide-aperture) azimuthal energy concentrations.

Besides demonstrating results on synthesized data, our anisotropy analysis is applied to real data. Peaks are extracted from data and attributed with a degree of anisotropy. The behavior of the peak attribution is consistent with the results of the synthetic data. In particular, the anisotropy characterization of geometric scatterers is consistent between narrow and wide-aperture settings when the underlying anisotropy is included in both hypothesis sets. Furthermore, in the wide-aperture setting with the augmented hypothesis set, we obtain a more detailed anisotropy characterization for smaller scatterers. A reduction in the rate of volumetric anisotropy with larger apertures is also observed using the real data.

The results presented here show a great deal of promise for the use of wide-aperture data. This benefit does not necessarily arise from simply using higher resolution imagery in existing ATR algorithms but comes from exploiting previously ignored anisotropy information. Not only can this information aid existing algorithms by providing better reflectivity estimates but also by characterizing scatterer stability as one can tell with more confidence which peak extractions are due to stable geometric scattering. Furthermore, the anisotropy information itself is a useful feature in ATR as this information allows one to infer properties of the underlying scatterer geometry.

Appendix A. Anisotropy Statistic Accounting for Neighboring Scatterers

In this Appendix, we present the details in extending the isolated scatterer anisotropy test to account for the presence of interfering scatterers by generalizing the model in Eq. (4) to explicitly include multiple scatterers. First, however, we must generalize the sub-aperture scattering model to account for the modulations produced by neighboring scatterers. Again, we assume that the sub-aperture measurements have been formed while being focused on a particular cross-range location y_0. The possibility of other scatterers are considered at discrete locations $y_0 + k\Delta_p$, where Δ_p specifies a cross-range sampling resolution for interfering scatterers. To model the effect of a scatterer with anisotropy H_{m_k,i_k} at location $y_0 + k\Delta_p$ on the measurements at location y_0, we simply modulate the azimuthal response $1_{H_{m_k,i_k}}(\cdot)$ to account for the shift in the image domain. The observed effect over the smallest sub-apertures is then given by

$$b^k(m_k, i_k)_j = \int_{S_{M,j}} e^{j2\pi \frac{k\Delta_p}{\Delta_r} t} 1_{H_{m_k, i_k}}(t)\, dt \tag{11}$$

where Δ_r is the null-to-null cross-range resolution associated with the full-aperture. Incorporation of the neighboring scatterers is now modeled via superposition, i.e.

$$\boldsymbol{q}_M = \sum_k A_k \boldsymbol{b}^k(m_k, i_k) + \varepsilon \tag{12}$$

where the noise model is the same as in Eq. (5). The summation over k in Eq. (12) should be over a range large enough to include all scatterers contained in the coarsest resolution cell, i.e. the resolution cell associated with the smallest sub-apertures. Thus, if L_* is the smallest aperture length, then we need to consider $k \in \{-K, \ldots, K\}$ where

$$\begin{aligned} 2K\Delta_p &\geq \frac{\Delta_r}{L_*} = \text{size of coarest resolution cell} \\ K &\geq \left\lceil \frac{\Delta_r}{2L_*\Delta_p} \right\rceil \end{aligned} \tag{13}$$

and $k = 0$ corresponds to the resolution cell under investigation. Rewriting Eq. (12) as a matrix equation we get

$$\begin{aligned} \boldsymbol{q}_M &= \left[\boldsymbol{b}^{-K}(m_{-K}, i_{-K}) \quad | \cdots | \quad \boldsymbol{b}^K(m_K, i_K) \right] \begin{bmatrix} A_{-K} \\ \vdots \\ A_K \end{bmatrix} + \varepsilon \\ &= B\boldsymbol{A} + \varepsilon \end{aligned} \tag{14}$$

where B and A are appropriately defined[16]. Thus, we can use weighted least squares (WLS) to implicitly estimate the values of the interfering A_k and account for their contribution to $\boldsymbol{q}_M$. In order to have our least squared error minimization correspond to ML, we weight our inner product by the inverse of the noise covariance to whiten the measurements, i.e. $\langle \boldsymbol{u}, \boldsymbol{v} \rangle = \frac{1}{2\sigma^2} \boldsymbol{u}^T \Lambda^{-1} \boldsymbol{v}$. The ML estimate for $\boldsymbol{A}$ is obtained from this model as

$$\hat{\boldsymbol{A}} = \arg \min_{\boldsymbol{A}} \; \{ \|\varepsilon\|^2_{\Lambda^{-1}} \} = (B' \Lambda^{-1} B)^{-1} B' \Lambda^{-1} \boldsymbol{q}_M$$

which simplifies to Eq. (6) in the case of limiting the model order to $K = 0$. One would like to then use ML to classify the anisotropy of the $k = 0$ scatterer, i.e. choose the sub-aperture hypothesis which minimizes the weighted norm of the estimated error $\varepsilon = \boldsymbol{q}_{Mz} - B\hat{\boldsymbol{A}}$. The model in Eq. (12), however, has too many reflectivity parameters and thus results in an under-constrained minimization problem. In particular, if one chooses K sufficiently large to account for all scatterers in the coarsest resolution cell, then the model order is greater than the number of sub-aperture measurements and the estimated $\hat{\varepsilon}$ can be made zero for all hypotheses. Thus, we need to regularize the model. In order for the estimated error $\hat{\varepsilon}$ to be made small under the incorrect model, many of the values in $\boldsymbol{A}$ generally have to be made unreasonably large and result in an unrealistic scenario. Thus, we impose a 2-norm regularization penalty in the estimation of $\boldsymbol{A}$. In particular, instead of minimizing the weighted squared error to estimate $\boldsymbol{A}$, we take as our estimate

$$\begin{aligned}\hat{\boldsymbol{A}} &= \arg\min_{\boldsymbol{A}} \{ \|\varepsilon\|^2_{\Lambda^{-1}} + \gamma \boldsymbol{A}' R \boldsymbol{A} \} \\ &= (B'\Lambda^{-1}B + \gamma R)^{-1} B'\Lambda^{-1}\boldsymbol{q}_M \\ &= P\boldsymbol{q}_M \end{aligned} \tag{15}$$

where P is defined accordingly, γ is the regularization parameter, and R is the regularization matrix that penalizes the energy in all A_k other than $k = 0$, i.e.

$$R = \boldsymbol{I} - \boldsymbol{e}_K\boldsymbol{e}'_K = \mathrm{diag}(1, \ldots, 1, 0, 1, \ldots, 1).$$

This regularized estimate for A produces the following value for the weighted norm on the error estimate

$$\begin{aligned}\|\hat{\varepsilon}\|^2_{\Lambda^{-1}} &= \|\boldsymbol{q}_M - B\hat{\boldsymbol{A}}\|^2_{\Lambda^{-1}} \\ &= \frac{1}{2\sigma^2}\boldsymbol{q}'_M\left[\Lambda^{-1} - 2\Lambda^{-1}BP + P'B'\Lambda^{-1}BP\right]\boldsymbol{q}_M \end{aligned} \tag{16}$$

which can be used as the sufficient statistic $\ell_{m,i}$ for our hypothesis test as this statistic corresponds to a generalized log-likelihood with a Gaussian prior on the neighboring reflectivities.

Although the norm in Eq. (16) is a statistic which can be easily calculated, there are an excessively large number of extended-hypotheses for which the test statistic needs to be computed. In particular, if we allow $2K$ neighboring scatterers, the number of candidate extended-hypotheses is now $\mathcal{H}^{2K+1}$ since each location has an associated scatterer and corresponding anisotropy hypothesis. For the initial work presented in this paper, we restrict our attention to hypotheses where only the anisotropy for the focused resolution cell under investigation is allowed to vary. In particular, the hypothesis for each of the $2K$ neighboring pixels is fixed to be full-aperture anisotropy while all hypotheses for the focused location are tested. Thus, we escape the exponential growth in the number of hypotheses since our hypothesis space is effectively still $\mathcal{H}$. Certainly, this constraint can be relaxed in order to appropriately take into account the anisotropy of neighboring scatterers, but we do not do so here[17]. We make special note that although the model for neighboring scatterers is restricted to full-aperture scattering, this multiple scatterer model is more powerful than the isolated scatterer model presented in Section 3.1 as the latter does not explicitly consider *any* interference from neighboring scatterers.

Notes

1. Correspondence should be sent to: Andrew Kim.
2. We will refer to anisotropy due to geometric scatterers as *geometric anisotropy* and anisotropy due to volumetric scatterers as *volumetric anisotropy*.
3. For clarity, we will exclusively use the term "cross-range" when referring to cross-range in the spatial (image) domain, and we will exclusively use the term "azimuthal" when referring to the corresponding dimension in the sensor domain.
4. By azimuthal response, we mean the 1-D cross-range uncompressed signal for a given down-range location. The signal $a(t)$ is assumed to have already been appropriately demodulated to have zero phase modulation for the inspected cross-range location.
5. The lack of normalization simplifies the notation in what follows later.
6. To be precise, it is actually the mean-squared reflectivity estimate normalized by the variance of the estimate that decreases as too much of the aperture is used. The estimator variance itself actually decreases because the coherent averaging is done over a larger aperture, but the squared-mean of the estimate decreases even more so since no additional signal energy is being incorporated.
7. The details of the multiple scatterer model, and the derivation of the resulting statistic can be found in Appendix A.
8. The term "sidelobes" here refers to those on a sinc-like function and *not* those associated a neighboring scatterer.
9. A comparison between the test based on the multiple scatterer model and the test from the isolated scattering model can be found in Chapter 5 of Kim [8].
10. The hypotheses thus correspond to isotropic (i.e. constant over the full 2.8° aperture), half-aperture (1.4°), and quarter-aperture (0.7°) anisotropy.
11. These other ripples are too small to be seen on this plot but are apparent if the noise level is increased or the scaling of the vertical axis is changed.
12. For each Monte Carlo trial, the peak extraction step detects local maximum in the log-magnitude reflectivity image and refines the scattering center location using parabolic interpolation.
13. This sub-aperture pyramid does not have the full-aperture at the root, however, all the previous analysis in Section 3 still applies. We note that the use of this "cropped" pyramid is solely to aid our comparison of narrow and wide-aperture data. In applied settings, we recommend that the full-aperture always reside at the root node to make maximum use of the aperture.
14. Note that there is also the issue of consistency of the peak locations. In order to overcome this problem, we first estimate the coarse-resolution peak location and then limit the high-resolution peak location to reside within the resolution cell corresponding to the coarse-resolution extraction.
15. The coarse resolution is used for the wide-aperture case (even though a finer imaging resolution can be achieved) due to publishing restrictions on this data.
16. Although the matrix B clearly depends on the extended-hypothesis $\{(m_{-K}, i_{-K}), \ldots, (m_K, i_K)\}$, this dependence is omitted for notational simplicity.
17. Research along this direction can be found in Chapter 7 of the thesis by Kim [8].

References

1. M. Allen, D. Sofianos, and L. Hoff, "Wide-Angle Wideband SAR Matched Filter Image Formation for Enhanced Detection Performance," in *Proc. of the SPIE, Algorithms for SAR Imagery*, vol. 2230, Apr. 1994, pp. 302–314.

2. R. Chaney, A. Willsky, and L. Novak, "Coherent Aspect-Dependent SAR Image Formation," in *Proc. of the SPIE, Algorithms for SAR Imagery*, vol. 2230, Apr. 1994, pp. 256–274.
3. J. Capon, "High-Resolution Frequency-Wavenumber Spectrum Analysis," in *Proc. IEEE*, vol. 57, no. 8, Aug. 1969, pp. 1408–1418.
4. G. Benitz, "Adaptive High-Definition Imaging," in *Proc. of the SPIE, Algorithms for SAR Imagery*, vol. 2230, Apr. 1994, pp. 106–119.
5. G. Benitz and D. DeLong, "Extensions of High Definition Imaging," in *Proc. of the SPIE, Algorithms for SAR Imagery*, vol. 2487, Apr. 1995, pp. 165–180.
6. "MSTAR (Public) Targets: T-72, BMP-2, BTR-70, SLICY", see http://www.mbvlab.wpafb.af.mil/public/MBVDATA.
7. A. Kim, *Exploring Scatterer Anisotropy in Synthetic Aperture Radar via Sub-Aperture Analysis*, PhD thesis, Massachusetts Institute of Technology, Sept. 2001.
8. A. Kim, J. Fisher, A. Willsky, and P. Viola, "Nonparametric Estimation of Aspect Dependence for ATR," in *Proc. of the SPIE, Algorithms for SAR Imagery*, vol. 3721, Apr. 1999, pp. 332–342.
9. H. Chiang and R. Moses, "ATR Performance Prediction Using Attributed Scattering Features," in *Proc. of the SPIE, Algorithms for SAR Imagery*, vol. 3721, Apr. 1999, pp. 785–796.
10. A. Kim, S. Dogan, J. Fisher, R. Moses, and A. Willsky, "Attributing Scatterer Anisotropy for Model Based ATR," in *Proc. of the SPIE, Algorithms for SAR Imagery*, vol. 4053, Apr. 2000.
11. L. Potter and R. Moses, "Attributed Scattering Centers for SAR ATR," *IEEE Trans. on Image Proc.*, vol. 5, Jan. 1997, pp.79–91.